Fuel 280 (2020) 118623

Contents lists available at ScienceDirect

Fuel

journal homepage: www.elsevier.com/locate/fuel

Effects of heterogeneous flow on carbon conversion in gas-solid circulating fluidized beds

Markku Nikku[a,*], Hadi Bordbar[b], Kari Myöhänen[a], Timo Hyppänen[a]

[a] Laboratory of Modelling of Energy Systems, School of Energy Systems, Lappeenranta University of Technology, Finland
[b] Laboratory of Fire Safety Engineering, Department of Civil Engineering, Aalto University, Finland

GRAPHICAL ABSTRACT

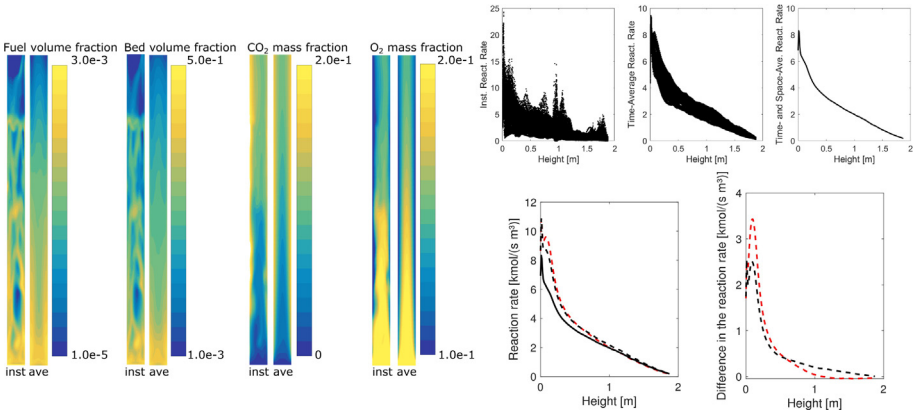

ARTICLE INFO

Keywords:
Fluidized bed
Combustion
Eulerian multiphase
CFD modeling
Reactivity
Mass transfer

ABSTRACT

Gas-solid fluidized beds have heterogeneous flow structures, which affect the reactions due to uneven distribution and limited mixing of reactants. Some model approaches neglect these heterogeneous structures and use a homogeneous assumption instead. This work demonstrates the effects of neglecting this heterogeneity. Eulerian multiphase modeling is utilized to model fuel conversion in a fluidized bed riser. The effects of the chemical reactivity of the fuel, the amount of fuel in the reactor and the fluidization regime are investigated. The model data are time- and space-averaged into 1D results and compared with a 1D modelling which assumes homogeneous distributions in radial direction. Based on this study, the negligence of the heterogeneous flow structures leads to significantly higher local and overall reaction rates and conversion in the system.

1. Introduction

Gas-solid fluidized beds are widely used in different industrial applications such as combustors, where large heat or mass transfer rates are desired [1]. The heat and mass transfer and thermochemical reactions appear on multiple time- and length-scales and a good understanding of these is essential for the design and analysis of fluidized bed processes. The heterogeneous nature and the strong coupling between the previously mentioned phenomena make fluidized beds challenging to study, both experimentally and with numerical models.

* Corresponding author.
E-mail address: mnikku@lut.fi (M. Nikku).

https://doi.org/10.1016/j.fuel.2020.118623
Received 28 June 2019; Received in revised form 30 June 2020; Accepted 3 July 2020

Nomenclature

A	area m^2
a_c	apparent surface area of fuel particles per volume m^{-1}
C	concentration mol m^{-3}
C_D	drag coefficient –
D_m	mass diffusion coefficient m^2 s^{-1}
d_p	particle diameter m
e	coefficient –
F	body force kg m^{-2} s^{-2}
f	quantity –
g	gravitational acceleration m s^{-2}
g_0	radial distribution –
H	heterogeneity; relative difference in reaction rates –
h	height m
h_m	mass transfer coefficient m s^{-1}
I	second invariant of the deviator of the strain rate tensor s^{-2}
J	diffusion flux kg m^{-2} s^{-1}
K	momentum transfer coefficient kg m^{-3} s^{-1}
k	chemical reactivity m s^{-1}
k_{eff}	effective reaction rate m s^{-1}
M	molar mass kg mol^{-1}
p	pressure Pa
q_m	mass flow rate kg s^{-1}
R	reaction source term mol m^{-3} s^{-1}
Re	Reynolds number –
S	source term kg m^{-3} s^{-1}
Sc	Schmidt number –
Sh	Sherwood number –
t	time s
V	volume m^3
v	velocity m s^{-1}
X	conversion ratio –
Y	mass fraction of species –
y	volume fraction of species in phase –
ε	volume fraction–
λ	bulk viscosity Pa s
μ	viscosity kg s^{-1} m^{-1}
τ	stress tensor Pa
ρ	density kg m^{-3}
θ	granular temperature m^2 s^{-2}
κ	granular conductivity kg m^{-1} s^{-1}
γ	dissipation of granular energy kg m^{-3} s^{-1}

Subscripts

0	superficial, initial
0D/1D/2D/3D	zero/one/two/three-dimensional
b	bed
f	fuel
fri	frictional
g	gas
het	heterogeneous
hom	homogeneous
i	index
m	mass
s	solid
ss	restitution between solid phases
x,y,z	dimensions

One challenge in the numerical modeling is finding the balance between the model accuracy and applicability.

The Eulerian-Eulerian (e.g. kinetic theory of granular flow) and Eulerian-Lagrangian (e.g. multiphase particle-in-cell) methods are commonly applied for pilot-scale to industrial-scale simulations [2]. This work concentrates on the Eulerian-Eulerian (E-E) approach, where both the gas and the particle phases are considered continuous. In the E-E approach, the mesh resolution needs to be sufficiently fine to capture the *meso*-scale features of multiphase flows. Sometimes mentioned rule-of-thumb for the size of the calculation cell is in the order of ten times the particle diameter [3]. For practical studies of industrial-scale systems, the mesh resolution needs to be considerably coarser to achieve reasonable calculation times. Moreover, the time-dependent simulations are usually simulated only for a short process time, in the order of few minutes, for obtaining data for representable averages [4–8]. The computational cost can be further reduced by using longer time steps or applying a steady-state solution method [9,10]. Simplifying even further, the dimensionality of the simulated system can be reduced. Examples of this include 2D CFD models [11], 1D process models with [12–14] and without [15] division in to different flow regions, and 0D block models for plant level modeling [16].

Each simplification and averaging may lose information and introduce error in the solution. Time-averaging loses the fluctuations of the fluidized bed, whereas space-averaging (i.e. coarse meshes or reduced dimensions) makes the flow more homogeneous, which filters out the fine structures. While in a homogeneous system this would not matter, the fluidized beds are known for their fluctuating heterogeneous flow structures, such as bubbles in bubbling fluidized beds and denser particle groups, i.e. clusters, in the circulating fluidized beds (CFB). Heterogeneity in this work is considered as non-uniformity in the particle and gas species distribution within a horizontal cross-section, i.e. area perpendicular to the vertical axis of the riser. Using solid fuel combustion as an example, as the oxygen-carrying air is less likely to flow through dense particle concentrations, the gas is effectively bypassing parts of the solid fuel within these denser regions. A maldistribution of reactants due to this limited mixing reduces the amount of the reactions compared to the homogeneous mixture. In the averaging process the effect of heterogeneity on the reactions is not preserved and the reaction rates are likely to be higher similarly to the homogeneous models. Correction attempts have been made, for example in modeling of the momentum exchange between the phases, where sub-grid-scale models [17] are used. The effect of particle distributions on radiative heat transfer in CFBs was studied and models assuming homogeneous distributions were found to produce significant errors [18]. Similar corrections should be applied to reaction modeling.

Modeling of the reactions is often simplified, e.g. simulating overall reactions instead of elementary reactions and limiting the studied species. The mass transfer related to reactions is characterized with Sherwood number, and in fluidized beds this research is based on works of Frössling [19], Ranz and Marshall [20,21], Johnson [22] and Rowe et al [23] on the single droplets and particles. Kunii and Levenspiel [24], Gunn [25], and La Nauze et al [26] expanded this research to fixed and bubbling beds. Similar methods are applied to CFBs and reviewed by Breault [27]. Breault et al [28,29] developed a mass transfer model for a cluster in a riser. Zevenhoven et al [30] modeled mass transfer in CFB riser. Vollert et al [31] studied mass transfer in laboratory-scale CFB with NO oxidation. Cloete et al [32] modeled nickel oxide and methane reactions in a CFB reactor and Shuyan et al [33] modeled heat and mass transfer in clusters. Kashyap et al [34] measured and computed mass transfer from a laboratory-scale CFB. Varas et al [35] used time-averaged data from coupled CFD-DEM simulations on a CFB riser with a one-dimensional model to compute the mass transfer coefficients. Lu et al [36] modeled mass transfer within a single particle cluster.

This study investigates the modeled reaction rates in a small CFB reactor between homogeneous and heterogeneous distributions. Effects

of the fluidization regime, reactivity of the fuel and the fuel inventory are studied. Detailed 3D data is generated by transient 3D CFD simulations with Ansys Fluent 19.2. The CFD results are averaged in space and time to produce 1D steady-state results that include the effect of heterogeneity. The averaged CFD results are compared with one-dimensionally solved reaction rates that assume homogeneous distributions of reactants. Compared to the previous studies, for example by Varas et al [35], the reactions are solved dynamically together with the hydrodynamics, including the effects flow heterogeneity on the mass transfer. The results show that the negligence of the heterogeneous flow structures can lead to significantly higher local and overall reaction rates and conversion in the system. This highlights the importance of acknowledging the heterogeneity that is inherent in fluidized beds. The assumption of homogeneous distributions in one-dimensional CFB models is still in use [37–39], especially as a first step in designing and studying new fluidized bed processes, thus one contribution of this work is to demonstrate the risks involved with applying such an approach.

2. Modeling

2.1. Eulerian CFD model

This work utilizes a three phase Eulerian modeling approach. The gas phase consists of N_2, O_2 and CO_2. For simplicity, the fuel phase is considered as pure carbon while the bed phase is modeled as inert. The gas phase is modeled as laminar and no separate turbulence models are applied for the solids phases.

The equations in this section are based on [40]. The continuity equations for the gas (g) phase and for the fuel (f) and bed (b) phases are given as

$$\frac{\partial}{\partial t}(\varepsilon_g \rho_g) + \nabla\cdot(\varepsilon_g \rho_g \boldsymbol{v}_g) = q_{m,fg} \tag{1}$$

$$\frac{\partial}{\partial t}(\varepsilon_b \rho_b) + \nabla\cdot(\varepsilon_b \rho_b \boldsymbol{v}_b) = 0 \tag{2}$$

$$\frac{\partial}{\partial t}(\varepsilon_f \rho_f) + \nabla\cdot(\varepsilon_f \rho_f \boldsymbol{v}_f) = -q_{m,fg} \tag{3}$$

where $q_{m,fg}$ represents the mass exchange term between the fuel and gas phases due to oxidation of the fuel carbon to gaseous CO_2. The conservation of momentum for different phases are given as

$$\frac{\partial}{\partial t}(\varepsilon_g \rho_g \boldsymbol{v}_g) + \nabla\cdot(\varepsilon_g \rho_g \boldsymbol{v}_g \boldsymbol{v}_g) = -\varepsilon_g \nabla p + \nabla\cdot\bar{\bar{\tau}}_g + \varepsilon_g \rho_g \boldsymbol{g} + \sum_s K_{sg}(\boldsymbol{v}_s - \boldsymbol{v}_g) + q_{m,fg}\boldsymbol{v}_f + \boldsymbol{F}_g \tag{4}$$

$$\frac{\partial}{\partial t}(\varepsilon_b \rho_b \boldsymbol{v}_b) + \nabla\cdot(\varepsilon_b \rho_b \boldsymbol{v}_b \boldsymbol{v}_b) = -\varepsilon_b \nabla p - \nabla p_b + \nabla\cdot\bar{\bar{\tau}}_s + \varepsilon_b \rho_b \boldsymbol{g} + K_{gb}(\boldsymbol{v}_g - \boldsymbol{v}_b) + K_{fb}(\boldsymbol{v}_f - \boldsymbol{v}_b) + \boldsymbol{F}_b \tag{5}$$

$$\frac{\partial}{\partial t}(\varepsilon_f \rho_f \boldsymbol{v}_f) + \nabla\cdot(\varepsilon_f \rho_f \boldsymbol{v}_f \boldsymbol{v}_f) = -\varepsilon_f \nabla p - \nabla p_f + \nabla\cdot\bar{\bar{\tau}}_s + \varepsilon_f \rho_f \boldsymbol{g} + K_{fg}(\boldsymbol{v}_g - \boldsymbol{v}_f) + K_{fb}(\boldsymbol{v}_b - \boldsymbol{v}_f) - q_{m,fg}\boldsymbol{v}_f + \boldsymbol{F}_f \tag{6}$$

The stress tensor of the phases ($s = f, b$) is given as,

$$\bar{\bar{\tau}}_g = \mu_g \varepsilon_g (\nabla \boldsymbol{v}_g + \nabla \boldsymbol{v}_g^T) + \frac{2}{3}\mu_g \varepsilon_g (\nabla\cdot\boldsymbol{v}_g)\bar{\bar{I}} \tag{7}$$

$$\bar{\bar{\tau}}_s = \mu_s \varepsilon_s (\nabla \boldsymbol{v}_s + \nabla \boldsymbol{v}_s^T) + \varepsilon_s(\lambda_s - \frac{2}{3}\mu_s)(\nabla\cdot\boldsymbol{v}_s)\bar{\bar{I}} \tag{8}$$

Appendix 1 presents the models applied in the kinetic theory of granular flows and momentum exchange modeling applied in this work.

The conservation equation for species i in the gas phase is given as

$$\frac{\partial}{\partial t}(\rho_g Y_i) + \nabla\cdot(\rho_g \boldsymbol{v}_g Y_i) = \nabla\cdot\boldsymbol{J}_i + S_i \tag{9}$$

where Y_i is the mass fraction of species and S_i is the source term from chemical reactions. Ignoring the thermal diffusion, the diffusion flux $\mathbf{J}_i$ arises from concentration gradients according to Fick's law as

$$\boldsymbol{J}_i = -\rho D_{m,i} \nabla Y_i \tag{10}$$

where $D_{m,i}$ is the mass diffusion coefficient for species i in the mixture.

2.2. Reaction model in CFD

The reaction modeling is applied similarly to Vepsäläinen et al [41]. The carbon combustion is simplified to primary oxidation reaction of C (solid) + O_2 (gas) → CO_2 (gas). The reaction model is volumetric laminar finite-rate, and the reaction rate is defined by the first-order rate function R.

$$R = a k_{eff} C_{O_2} \tag{11}$$

where C_{O2} is the molar concentration of oxygen. The surface area of fuel per reactor volume is

$$a = 6\frac{\varepsilon_f y_f}{d_{p,f}} \tag{12}$$

where y_f is the volume fraction of carbon within the fuel phase. The effective reaction rate k_{eff} coefficient including the effect of chemical kinetics k_f and mass transfer is defined as

$$k_{eff} = \frac{1}{\frac{1}{k_f} + \frac{1}{h_m}} \tag{13}$$

The local convective mass transfer coefficient h_m is computed with Eq. (14) by using correlation in Eq. (15) for the Sherwood number with the local gas volume fraction and particle Reynolds number,

$$h_m = \frac{\mathrm{Sh}\, D_{m,O_2}}{d_{p,f}} \tag{14}$$

$$\mathrm{Sh} = 2\varepsilon_g + 0.69\left(\frac{\mathrm{Re}}{\varepsilon_g}\right)^{0.5} \mathrm{Sc}^{1/3} \tag{15}$$

where D_{O2} and $d_{p,f}$ present the diffusivity of oxygen and the diameter of the fuel particle, respectively.

2.3. CFD case setup

Fig. 1 presents the geometry, 3D mesh and its 1D representation.

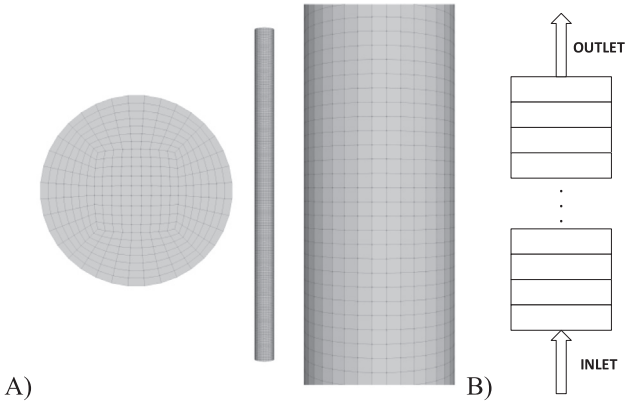

Fig. 1. A) The used geometry with close ups of the mesh from the side and bottom. B) The 1D model. C) Comparison of the measured and CFD modeled pressure profiles.

The riser height is 1.8 m and diameter 0.11 m. The mesh size was 66.000 cells, with an average cell size of 10 particle diameters. The model setup follows the values reported by Shah et al [42]. The hydrodynamical model frame was previously validated with measurements by Nikku et al [43], and a comparison of pressure profile results in an ambient temperature case without the fuel phase is presented in Fig. 1C. A good agreement was achieved between the measurements and the hydrodynamic model, similarly with the same hydrodynamical modeling approach validation on other cases for example by Nikku et al [44]. The simulations were performed in parallel processing with 16 cores.

The mass flow inlet boundary at the bottom is common for all the phases to eliminate the macroscopic mixing of reactants entering from different inlets and to set homogeneous distribution of gas and solid phases at the inlet. The bed and fuel have same properties to prevent segregation. The air mass flow rate was defined for a desired fluidization velocity. User defined functions (UDF) were used for keeping the mass of the bed material constant and for the reactivity modeling (Eqs. 11–15). Only the inert bed material was returned to the riser through the inlet, unlike the fuel exiting through the pressure outlet. A constant fuel feeding mass flow rate was applied to simplify the analysis of effects of different parameters. For gas, a no-slip, no-diffusion boundary condition was used at the riser walls, whereas for the solid phases a specularity coefficient of 0.01 was applied. An incompressible ideal gas law in isothermal conditions was used in computation of the gas density. Thus, the gas density varied only as a function of the chemical composition. This negates any differences in the hydrodynamical conditions arising from temperature distributions affecting the local gas properties, which allows for better parametric study between different cases. A constant temperature of 900 °C was assigned to all phases across the domain and constant values of 45×10^{-6} kg m^{-1} s^{-1}, and 132×10^{-6} m^2 s^{-1} were set for the gas viscosity and oxygen diffusivity, respectively. Other simulation settings are listed in Table 1.

From the initialization, the simulations were carried out until the flow fields and concentrations of fuel and species had stabilized. After this, the simulations were continued for a 30 s period and data was collected for time-averaging. In total, 18 cases were simulated, as shown in Table 2, to study the effects of fuel inventory, chemical reactivity of the fuel, and fluidization velocity.

2.4. Time- and space-averaging of CFD results

The CFD results from the time-averaging period were time- and space-averaged with following methods. The unweighted time-averaging was carried out for quantity f in each cell of the computational mesh as

$$\bar{f}_{x,y,z} = \frac{1}{\Delta t}\int_{\Delta t} f_{x,y,z}\,dt \tag{16}$$

The unweighted time-averaged quantities are space-averaged over the volume of identical cylindrical discs along the height of the riser to form a 1D representation of 3D data.

$$\bar{\bar{f}} = \frac{1}{\Delta V}\int_{\Delta V} \bar{f}_{x,y,z}\,dV \tag{17}$$

To take into consideration the heterogeneous species distributions and flow fields inside the riser and the cross-correlation of these quantities, mass flow weighted time- and space-averaging was used for the concentrations of the species. Hereafter, the double overbar indicates averaging over time and space

$$\bar{\bar{Y}} = \frac{1}{(\bar{\bar{\varepsilon}}\bar{\bar{\rho}}\bar{\bar{\mathbf{v}}})At}\int_A\int_{t_0}^{t_1} (\varepsilon\rho\mathbf{v}Y)_{x,y,z}\,dtdA \tag{18}$$

2.5. 1D reactivity modelling

While the effect of the 3D heterogeneous distributions on the reaction rates are obtained directly from the time- and space-averaged CFD results, a 1D model is used to calculate the carbon reaction rate with the assumption of homogeneous gas and particle distributions. Two different approach are taken, a 1D homogeneous approach, and a "3D" homogeneous approach. Both approaches are described in detail below.

In the 1D homogeneous approach, the Sherwood number with homogeneous distributions $\mathrm{Sh}_{1D,hom}$ is obtained with (Eq. (19)) using the CFD computed time- and space-averaged volume fractions, while computing the other variables from the boundary conditions and parameters common with the CFD modeling.

$$\mathrm{Sh}_{1D,hom} = 2\bar{\bar{\varepsilon}}_g + 0.69\left(\frac{\mathrm{Re}}{\bar{\bar{\varepsilon}}_g}\right)^{0.5}\mathrm{Sc}^{1/3} \tag{19}$$

$$\mathrm{Re}_{1D,hom} = \frac{d_p\rho_{g,1D}\mathbf{v}_{g,1D}}{\mu_{g,1D}} \tag{20}$$

where $\mathbf{v}_{g,1D} = \mathbf{v}_{g,0}/\bar{\bar{\varepsilon}}_g$. The mass transfer coefficient $h_{m\ 1D,hom}$, the effective reaction rate coefficient $k_{eff\ 1D,hom}$, and the carbon reaction rate $R_{1D,hom}$ are computed as follows.

$$h_{m\ 1D,hom} = \frac{\mathrm{Sh}_{1D,hom}D_{m,O_2}}{d_{p,f}} \tag{21}$$

$$k_{eff\ 1D,hom} = \frac{1}{1/k_f + 1/h_{m\ 1D,hom}} \tag{22}$$

$$R_{1D,hom} = k_{eff\ 1D,hom}\bar{a}\frac{Y_{O_2,1D}\rho_g}{M_i} \tag{23}$$

The reaction rate depends on the concentration of oxygen Y_{O2}. A steady state profile of oxygen is solved with a 1D conservation equation (Eq. (24)), which considers only the convection and the source term from the combustion reaction R, as the role of diffusion between the cells is negligible. The equations are solved by a finite volume method with first order upwind discretization scheme with boundary conditions in (Eq. (25)).

$$\frac{d(\rho_g\varepsilon_g v_g Y_{O_2})}{dz} = RM_{O_2} \tag{24}$$

$$\begin{cases} z = 0 \rightarrow Y = Y_0 \\ z = \max(h) \rightarrow dY/dz = 0 \end{cases} \tag{25}$$

The 3D homogeneous approach utilizes a similar 1D framework as described with (Eq. 19–23) for solving the reaction rates by using the time- and space-averaged CFD results of velocity, density, gas volume fraction, Reynolds number and oxygen concentration for each 1D plane. With this method, the reaction rates are computed in post-processing and they are not coupled back to the CFD computations. This method illustrates the error in the reaction rates when ignoring the local

Table 1
CFD model parameters.

Bed material and fuel particle diameter (mm)	0.5
Density of bed material and fuel particles (kg/m^3)	2465
Volume fraction at the inlet for bed material and fuel (–)	0.19, 0.01
Total mass of inert bed material in the riser (kg)	1.5
Angle of internal friction (°)	30
Packing limit (–)	0.63
Friction packing limit (–)	0.61
Coefficient of restitution (–)	0.9
Time step (s)	0.001
Number of iterations per time step	20

Table 2
The simulation cases, divided with the investigated parameter.

Reactivity	$\mathbf{v}_{g0}$ (m/s)	k_f (m/s)	$q_{m,f}$ (g/s)
R1	4.0	0.01	3.5
R2	4.0	0.02	3.5
R3	4.0	0.5	3.5
R4	4.0	1.0	3.5
Fuel mass	$\mathbf{v}_{g0}$ (m/s)	k_f (m/s)	$q_{m,f}$ (g/s)
F1	4.0	0.1	0.175
F2	4.0	0.1	0.35
F3	4.0	0.1	7.0
F4	4.0	0.1	35.0
F5	4.0	0.1	70.0
Fluidization velocity	$\mathbf{v}_{g0}$ (m/s)	k_f (m/s)	$q_{m,f}$ (g/s)
A1	4.0	0.01	35.0
A2	4.0	0.1	3.50
A3	4.0	1.0	0.35
C1	3.0	0.01	26.2
C2	3.0	0.1	2.62
C3	3.0	1.0	0.26
D1	5.0	0.01	43.6
D2	5.0	0.1	4.36
D3	5.0	1.0	0.44

variation of the reaction rates.

The reaction rates are compared between the 3D heterogeneous, 3D homogeneous and 1D homogeneous assumptions as well as comparing the species profiles of 3D heterogeneous and 1D homogeneous assumptions.

To quantify the level of heterogeneity affecting to the reactions, the simultaneous local concentrations of oxygen and fuel have to be considered as they both affect to the reaction rate and either of them can be the limiting factor. For comparison, the effect of homogeneously distributed quantities has to be acknowledged. The level of heterogeneity is defined as

$$H = \frac{R_{hom} - R_{het}}{R_{hom}} \tag{26}$$

The reaction rates are utilized in the definition to directly indicate the effect on the reactions, rather than an indirect approach utilizing the non-uniformity of oxygen and fuel concentrations, which would have to be cross-correlated together. This cross-correlation effect is acknowledged and visible in Eq. (11).

Total oxygen conversion, presented in Eq. (27), is defined from inlet and outlet values:

$$X_{O_2} = \frac{y_{O_2,in} - y_{O_2,out}}{y_{O_2,in}} \tag{27}$$

Oxygen conversion is used in instead of fuel, as the oxygen does not deposit in the reactor, unlike the fuel which forms an inventory. The role of the homogeneous 1D model is to produce perfectly homogeneous distributions in radial direction, rather than trying to represent the heterogeneity considering features such as division in to dense bed-freeboard [13] or core-annulus flow structure [14], thus, already attempting to mitigate the assumption of homogeneity in 1D models. The modeled cases represent fully homogeneous and heterogeneous approaches, with the results of intermediate modeling approaches (for example 1.5D, 2D) likely falling between the two presented approaches.

3. Results and discussions

Fig. 2 presents instantaneous profiles and the time-averaged contours of the volume fractions of fuel and bed, and CO_2 and O_2 mass fractions in a vertical cross-section for a single case (R1). The instantaneous figures show uneven distributions of gas species and solid phases. The time-averaged profiles are much smoother and symmetrical when compared with the instantaneous ones. Still, the species are not homogeneously distributed, the time-averaged concentrations of solid phases are higher near the wall and more dilute at the core, displaying the so-called core-annulus- flow structure. Fig. 3 presents the instantaneous and time-averaged Sherwood number and reaction source term distributions. The majority of the reactions take place in the bottom part of the riser and in the vicinity of the wall layer where the concentrations of fuel and oxygen are the highest. This can also be seen in profiles of O_2 as consumption and as production of CO_2. There is limited radial mixing of gas, visible as O_2 rich core and O_2 depleted wall layer, and vice versa with CO_2. This causes the highest time-averaged reaction source values to be located on the interface of high O_2 and fuel concentrations. The presented figures are case-specific, but they are still prime examples of the heterogeneity in fluidized beds that arise even

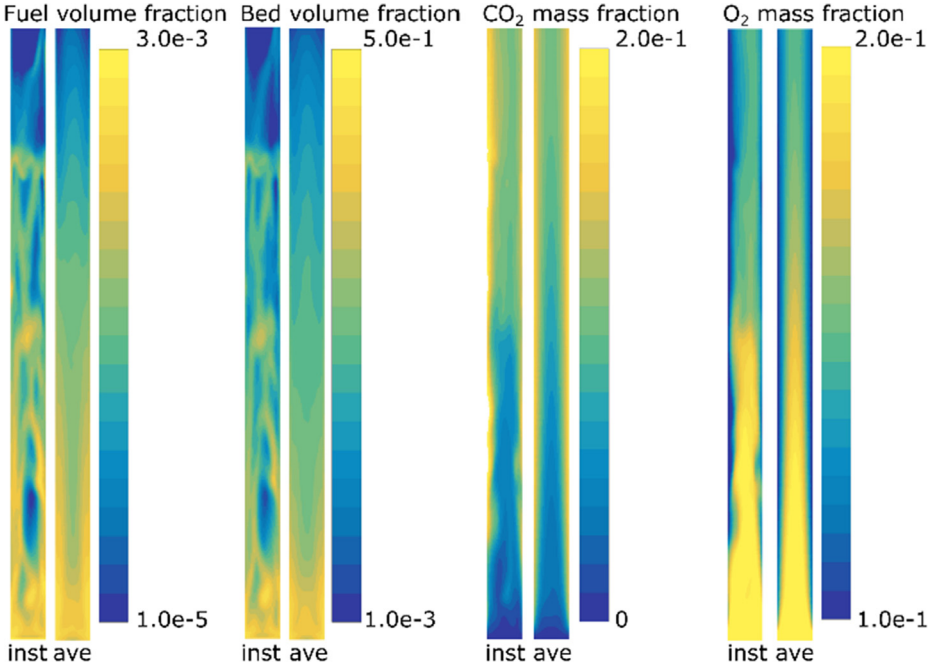

Fig. 2. CFD results of a single time step (inst) compared time-averaged (ave) results for volume fractions of fuel and bed, and species mass fractions of O_2 and CO_2.

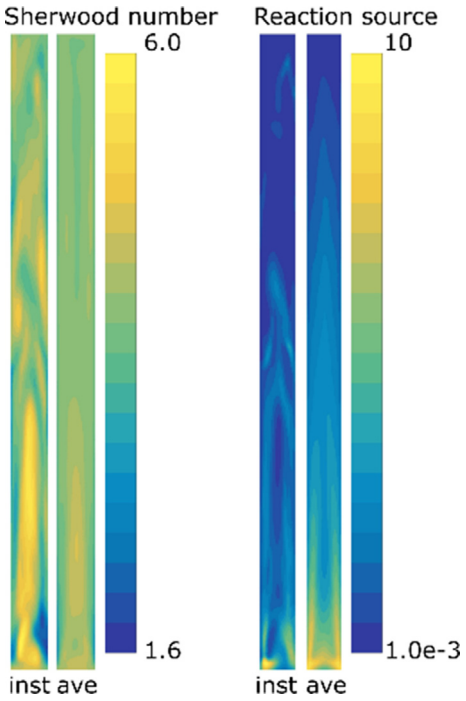

Fig. 3. CFD results of instantaneous (inst) and time-averaged (ave) Sherwood number and the reaction source term (kmol m^{-3} s^{-1}).

with homogeneous boundary conditions and without the modeling of turbulence.

Fig. 4 illustrates the variation of instantaneous reactions for each computational cell compared to the time and time- and space-averaged reaction rates. The instantaneous values show larger variations due to the spatial and temporal fluctuations in the concentrations of species and velocities. Time-averaging loses the fluctuations, hence, the variations are smaller. With the time- and space-averaged values there is no variation within a given height of the reactor, as the local values are lost and differences only exist between different heights. These averages still describe the overall process correctly, if the heterogeneity was originally considered. The following chapters show, how the results may change if the heterogeneity has not been correctly considered.

3.1. Effect of the chemical reactivity of the fuel

The effect of the chemical reactivity of the fuel is illustrated in Fig. 5 with five otherwise identical cases except for the chemical reactivity of the fuel (cases A2 and R1-R4). This shows how the higher reactivity leads to increased conversion as well as larger differences between the species profiles of the homogeneous and heterogeneous assumptions. The overall values are reported in Table 3. With low reactivity, the conversion is low and the majority of the fuel and oxygen are transported out of the reactor. In actual CFB reactors, the recirculation of the fuel would mitigate this problem.

The heterogeneity, defined as relative difference of reaction rates between the homogeneous and the heterogeneous results, increase with the chemical reactivity as seen on Table 3. The vertical distribution is visible in Fig. 6 through absolute differences in the reaction rates, where the absolute differences are utilized for the convenience of plotting. Larger reaction rates occur in the lower reactor where the concentrations of oxygen and fuel and the level of heterogeneity are high, with the reaction rates dropping higher in the riser due to limited fuel concentrations. Both homogeneous assumptions overestimate the local reaction rates compared to the heterogeneous assumption. The exceptions are cases of high reactivity, where the 1D homogeneous reactions in lower reactor consume majority of the oxygen resulting to lower reaction rates in upper riser than with the heterogeneous case. As the 3D homogeneous assumption computes the reaction rates using the O_2 concentrations from the CFD results, this approach is closer to the heterogeneous assumption results, while always overestimating the local reaction rate. The total conversion and reactor average reaction rates are always higher for both homogeneous assumptions.

The conversion is linearly proportional to the average reaction rate in the riser, which increases with a logarithmic relation with respect to the reactivity of the fuel. The increasing chemical reactivity reduces the fuel inventory in the system, which in general decreases the reaction rate (demonstrated in the following chapter), but this effect is negligible compared to the increased reaction rate due to the increasing chemical reactivity of the fuel. Fig. 7 presents the differences in the O_2 conversion between the assumptions. The differences are non-linear, with the $k_f = 0.1$ offering the largest difference of 14% and the differences decrease as the conversion approaches 0 or 1. This is expected, as the heterogeneity plays a smaller role in cases where the low chemical reactivity of the fuel is limiting the reactions. Similarly, in cases where the conversion with the homogeneous assumption is already close to the theoretical maximum, the results with homogeneous and heterogeneous assumption are approaching each other.

3.2. The effect of fuel inventory

The effect of the fuel inventory was studied by varying the inlet mass flow rate of the fuel and allowing the system to develop the fuel inventory and reach a pseudo-steady-state operations. As pointed out earlier, also the chemical reactivity of the fuel affects the formation of

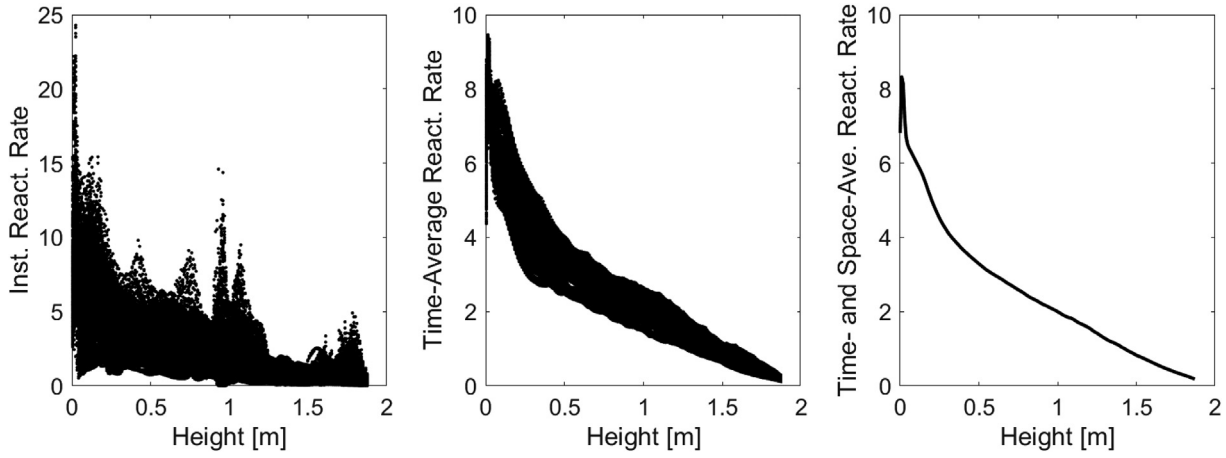

Fig. 4. Example of instantaneous, time-averaged and time- and space-averaged reaction rates in kmol m^{-3} s^{-1}.

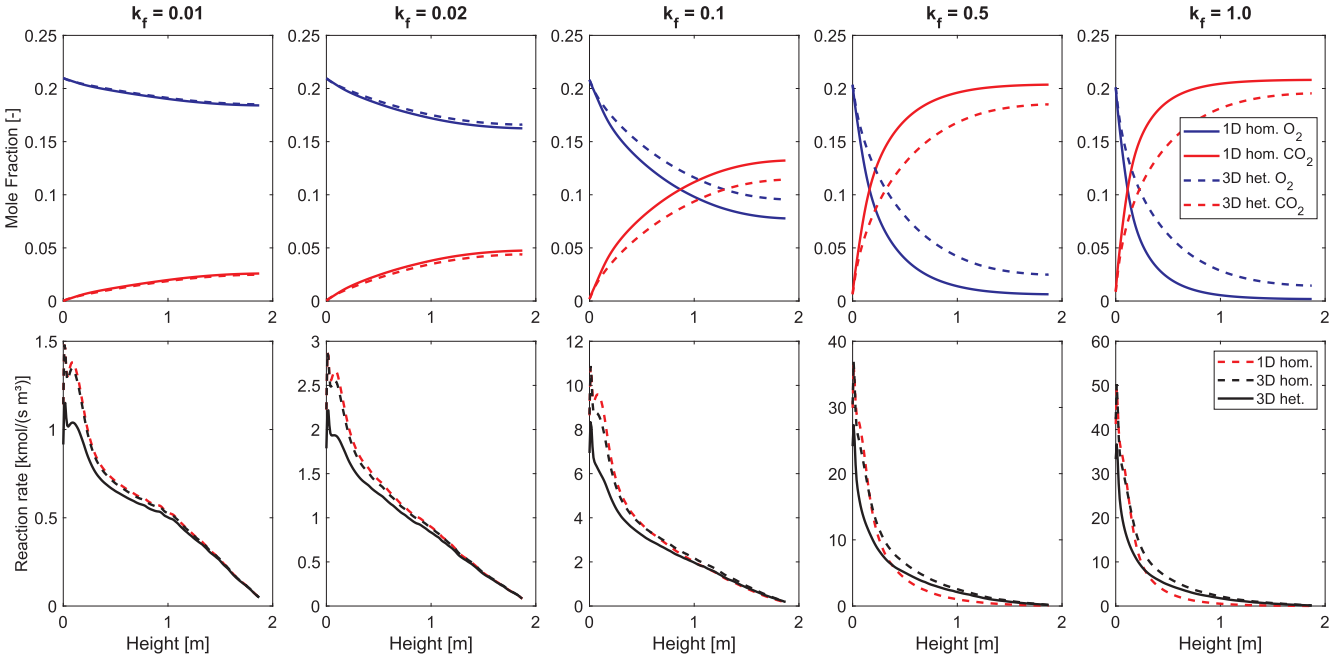

Fig. 5. The effect of the chemical reactivity of the fuel on the reaction rates with different assumptions.

Table 3
The effect of the chemical reactivity of the fuel on overall results.

Case	k_f (m/s)	m_f (g)	$Fuel_{out}/Fuel_{in}$ (–)	$X_{3D,het}$ (–)	$X_{1D,hom}$ (–)	$R_{3D,het}$ (kmol/(m^{3}s))	$R_{3D,hom}$ (kmol/(m^{3}s))	$R_{1D,hom}$ (kmol/(m^{3}s))	H_{3D} (–)	H_{1D} (–)
R1	0.01	104.5	0.99	0.118	0.124	0.513	0.567	0.576	0.095	0.110
R2	0.02	97.1	0.95	0.209	0.226	0.917	1.030	1.056	0.110	0.132
A2	0.1	85.5	0.82	0.543	0.630	2.514	2.921	2.943	0.139	0.146
R3	0.5	69.7	0.77	0.881	0.970	4.081	5.569	4.532	0.267	0.100
R4	1.0	71.0	0.72	0.933	0.991	4.326	6.166	4.631	0.298	0.066

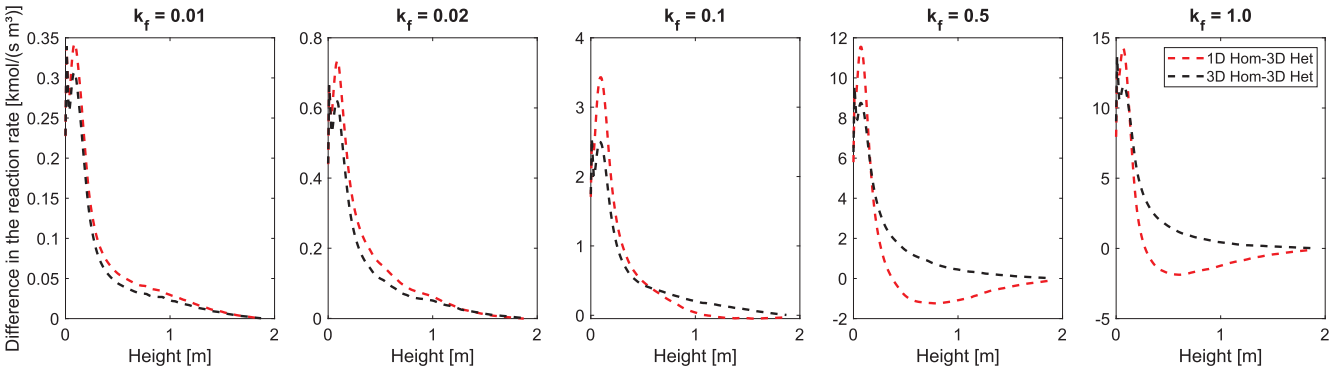

Fig. 6. The differences in reaction rates between homogeneous and heterogeneous assumptions with different reactivity of the fuel.

the fuel inventory, hence a constant chemical reactivity for the fuel was used. The results for cases A2 and F1-F5 are presented and compared in Fig. 8 with reaction rate and gas species profiles, Fig. 9 with differences between reaction profiles, Fig. 10 and Table 4 with reactor average and profiles of reaction rates, conversion and its differences between the assumptions. Increases in the fuel feeding cause a linear increase in the fuel inventory and a logarithmic increase in the share of the fuel exiting the reactor, the average reaction rates and conversion. The differences in the conversion with different assumptions increase rapidly at first, then reach a maximum and then decrease. This trend is clearly visible even with the limited amount of data points, similar to behavior observed in Fig. 7. The reasons for this behavior are similar, in cases with low amount of fuel, which leads to low conversion, the differences between the assumptions are small as mass transfer plays a minor role. As the reactor is saturated by fuel, the oxygen always finds plenty of fuel to react with, leading to high conversion with both assumptions and, as discussed earlier, large differences are not observed. Large local differences are observed in the reaction rate profiles, while the results over the reactor are highly similar. This is also visible from the heterogeneity level results of 1D homogeneous approach, which behaves similarly to conversion difference. The mass transfer plays the dominant role when the amounts of the reactants are more comparable with each other and mixing in the reactor is limiting the conversion.

3.3. The effect of gas velocity

The superficial fluidization velocity changes the reactor hydrodynamics significantly. Examples of the flow profiles for the 3 and 5 m/

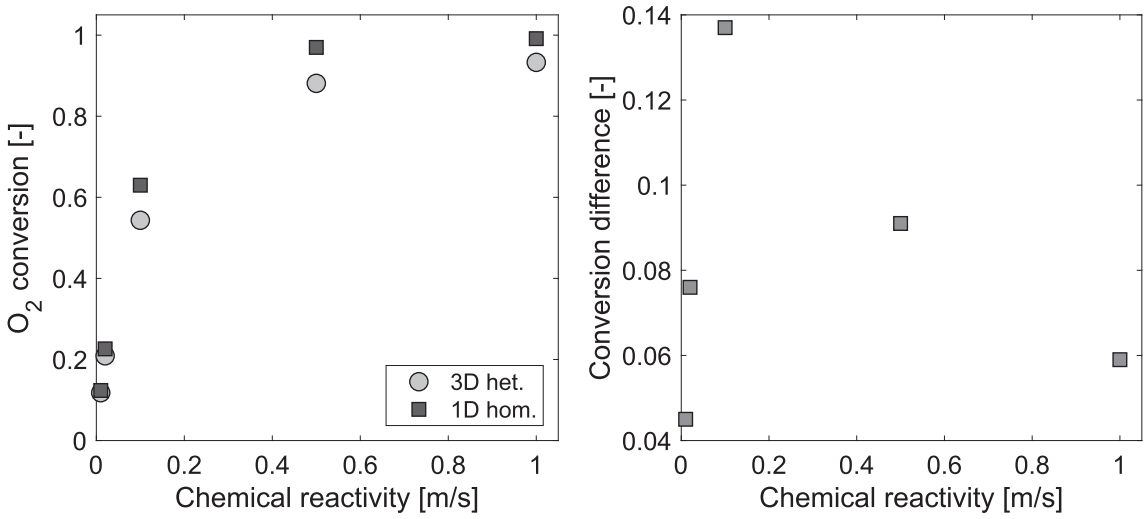

Fig. 7. Effects of chemical reactivity of the fuel on the oxygen conversion and conversion difference.

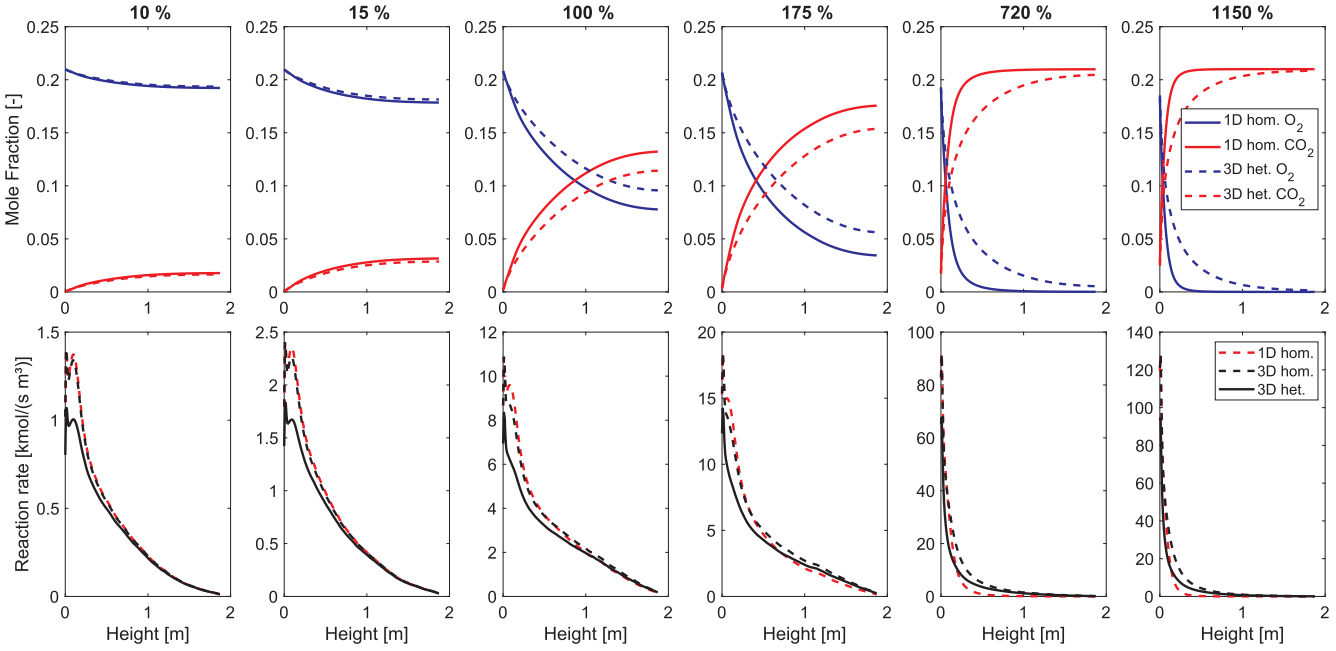

Fig. 8. The effect of the fuel inventory, with the fuel mass reported compared to the case A2 (100%). The reaction rates with different assumptions and the resulting oxygen and carbon dioxide profiles.

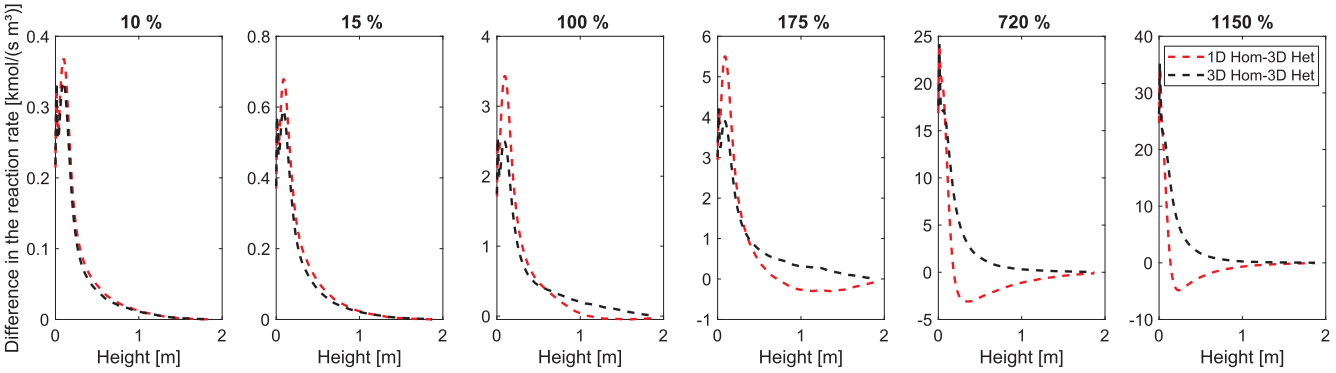

Fig. 9. The differences in reaction rates between the homogeneous and the heterogeneous assumptions with different fuel inventories.

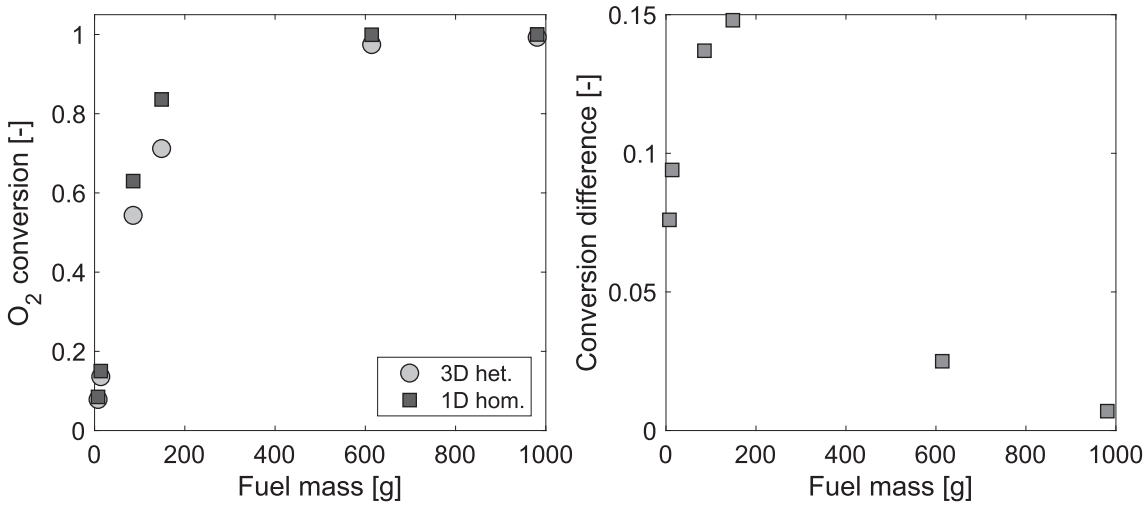

Fig. 10. Relation of fuel inventory to heterogeneous conversion and conversion difference.

Table 4
The effect of the fuel mass on the ratio of fuel exiting the reactor, oxygen conversion and averaged reaction rates.

Fuel mass	$q_{m,f}$ (g/s]	m_f (g)	$Fuel_{out}/Fuel_{in}$ (–)	$X_{3D,het}$ (–)	$X_{1D,hom}$ (–)	$R_{3D,het}$ (kmol/(m^{3}s))	$R_{3D,hom}$ (kmol/(m^{3}s))	$R_{1D,hom}$ (kmol/(m^{3}s))	H_{3D} (–)	H_{1D} (–)
F1	0.175	7.67	0.50	0.079	0.085	0.346	0.389	0.395	0.111	0.124
F2	0.35	13.7	0.63	0.136	0.150	0.593	0.686	0.701	0.136	0.154
A2	3.5	85.5	0.82	0.543	0.630	2.514	2.921	2.943	0.139	0.146
F3	7.0	148.5	0.85	0.712	0.836	3.344	4.108	3.907	0.186	0.144
F4	35.0	614.0	0.98	0.975	0.99935	4.544	6.937	4.752	0.345	0.044
F5	70.0	980.9	0.96	0.993	0.99999	4.638	7.531	4.674	0.384	0.008

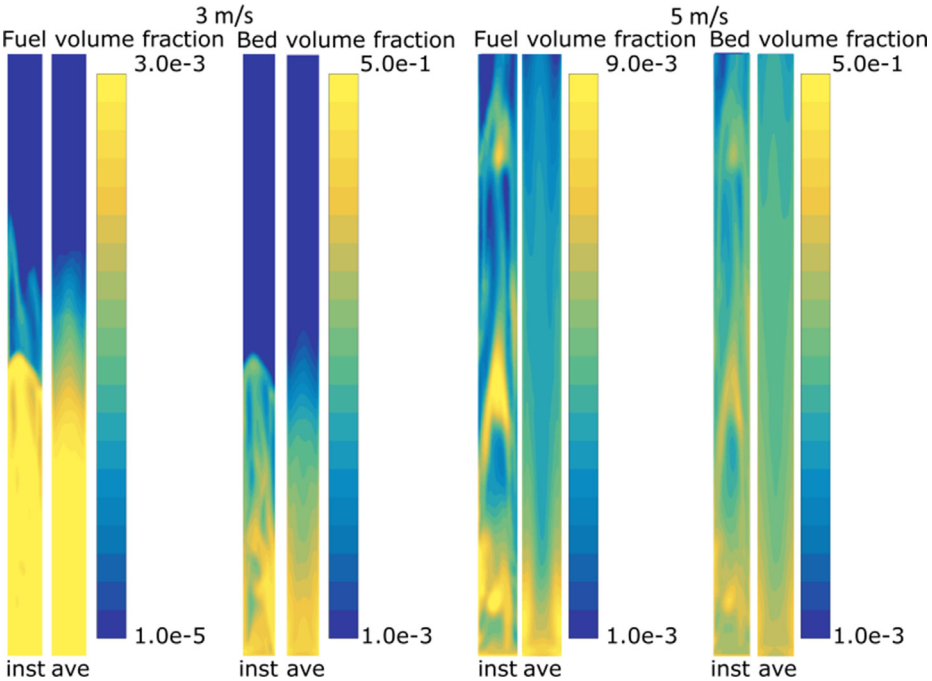

Fig. 11. Examples of the effects of the fluidization velocity on the CFD results of a single time step (inst) and time averaged (ave) results of volume fractions of fuel and bed, and species mass fractions of O_2 and CO_2.

s cases are presented in Fig. 11. Compared with Fig. 2, the 3 m/s cases represent a turbulent bed rather than a fast bed. In the 5 m/s case, the solid material is more evenly distributed vertically, with the solids and gas moving faster through the riser and having less time to react. The stoichiometry (molar ratio of oxygen to fuel) was kept constant between the different fluidization velocities, 0.029, 0.29 and 2.9, with respect to the changing chemical reactivity of the fuel of 0.01, 0.1 and 1.0 m/s. The resulting process parameters are presented in Table 5. High oxygen conversion is observed with 3 m/s cases, except with the highest chemical reactivity of the fuel, where the fuel inventory is very low and the amount of available fuel is limiting the conversion. For the 4 m/s cases, there are high shares of fuel exiting the riser and as well as low

Table 5
The effect of the fluidization velocity on the fuel inventory, ratio of fuel exiting the reactor, oxygen conversion and reactor averaged reaction rates. Cases 1 have k_f = 0.01, cases 2 k_f = 0.1 and cases 3 k_f = 1.0.

Case	v_{g0} (m/s)	m_f (g)	$Fuel_{out}/Fuel_{in}$ (–)	$X_{3D,het}$ (–)	$X_{1D,hom}$ (–)	$R_{3D,het}$ (kmol/(m^{3}s))	$R_{3D,hom}$ (kmol/(m^{3}s))	$R_{1D,hom}$ (kmol/(m^{3}s))	H_{3D} (–)	H_{1D} (–)
C1	3.0	3025	0.84	0.912	0.995	3.172	5.012	3.488	0.367	0.091
A1	4.0	660	0.99	0.487	0.577	2.181	2.658	2.694	0.182	0.192
D1	5.0	138	0.99	0.126	0.131	0.682	0.752	0.766	0.092	0.109
C2	3.0	1072	0.04	0.996	0.9999	3.493	5.974	3.505	0.415	0.003
A2	4.0	86	0.82	0.543	0.630	2.514	2.921	2.943	0.139	0.146
D2	5.0	20	0.96	0.157	0.172	0.856	0.979	1.004	0.126	0.147
C3	3.0	8	0.00	0.383	0.524	1.272	1.841	1.836	0.309	0.307
A3	4.0	6	0.24	0.294	0.360	1.289	1.658	1.680	0.223	0.233
D3	5.0	3	0.68	0.118	0.138	0.640	0.797	0.806	0.197	0.206

conversion values, and even further reduced reactor performance with 5 m/s due to faster elutriation of fuel. The reactor scale heterogeneity level vary with different combinations of reactivity and fluidization velocity with no clear trend.

Fig. 12 presents the differences in reaction rate profiles and Fig. 13 shows the changes in the O_2 profiles. Fig. 14 presents the effect of fluidization velocity on the O_2 conversion and the conversion differences between the assumptions. Differences with the O_2 and the reaction rate profiles are similar to previously presented. Homogeneous model produces larger local reaction rates in the dense region and the oxygen conversion is higher. The local reaction rates of the 1D homogeneous model can fall below the heterogeneous values, while the reactor average reaction rates are always higher with the homogeneous approaches. Increased chemical reactivity of the fuel reduced differences between the different velocities, though this effect is largely due to having more similar fuel inventories as well as the stoichiometry, which makes the cases more comparable. The mass transfer limitations are more clearly visible with the higher reactivity values, as the reactor is not saturated with fuel. Similarly, the differences between the homogeneous and heterogeneous assumptions are larger with 4 m/s, and the reduction in the differences with 5 m/s is related to the smaller fuel inventories, which reduced the role of mass transfer as observed in the previous chapter. Compared to 3 m/s, the conversion profiles of 4 and 5 m/s cases are more even as the reactions are also distributed to the upper parts of the riser.

Increases in the fluidization velocity reduce the fuel inventory and accelerate the fuel transport out of the reactor, which lowers the reaction rates and conversion. With the 5 m/s, a significant amount of

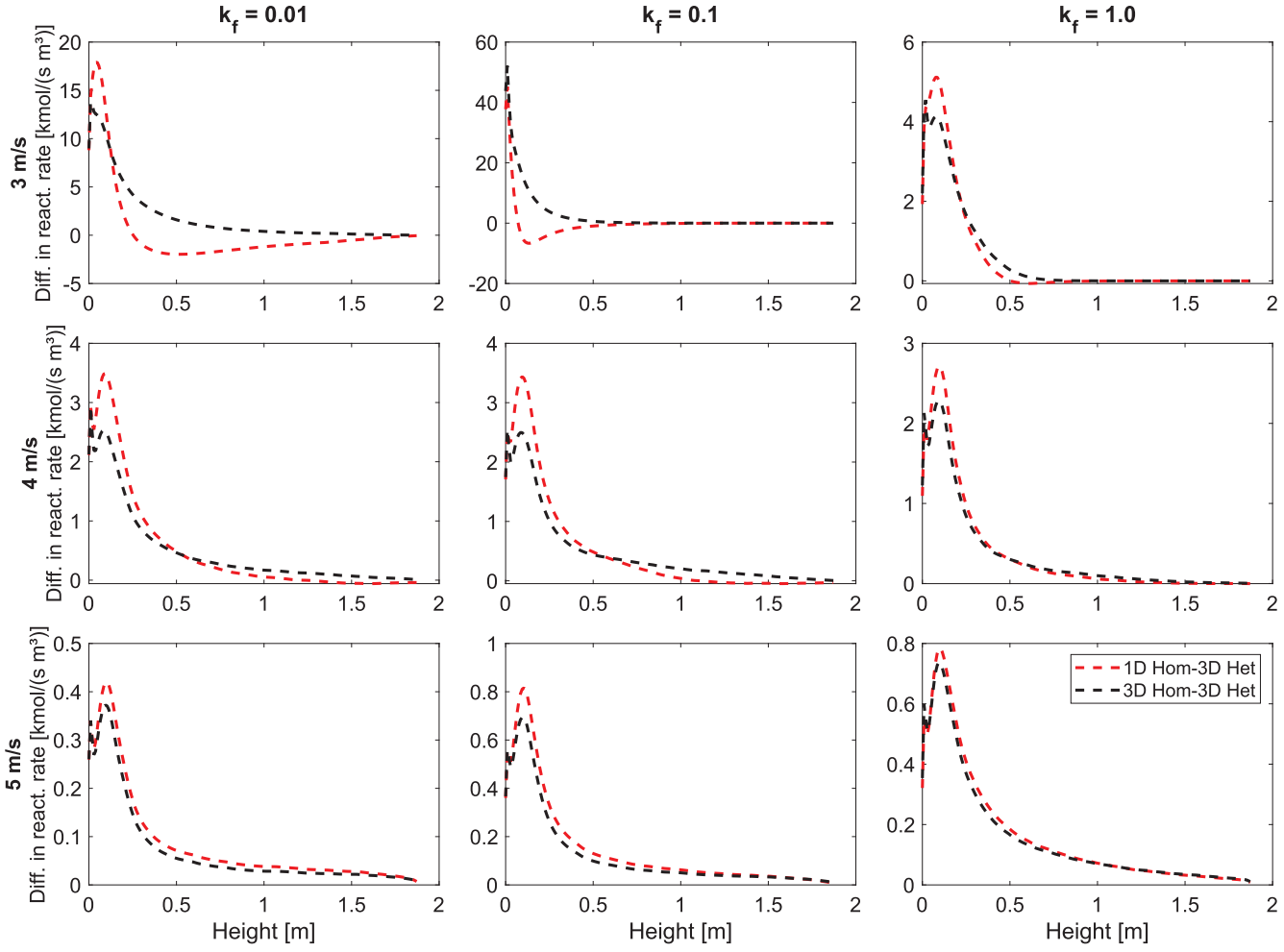

Fig. 12. The differences in reaction rates with different fluidization velocities and chemical reactivity values of the fuel.

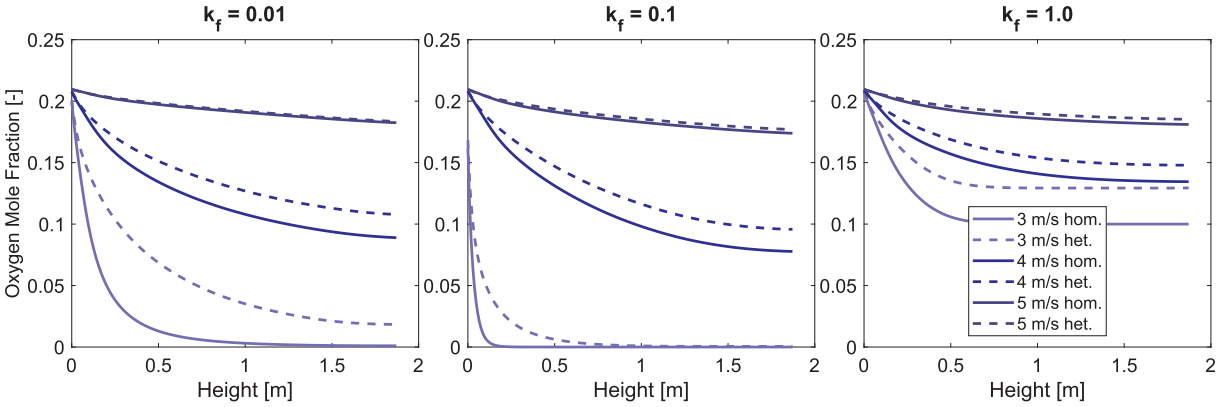

Fig. 13. The oxygen mass fraction profiles with different fluidization velocities and chemical reactivity of the fuel.

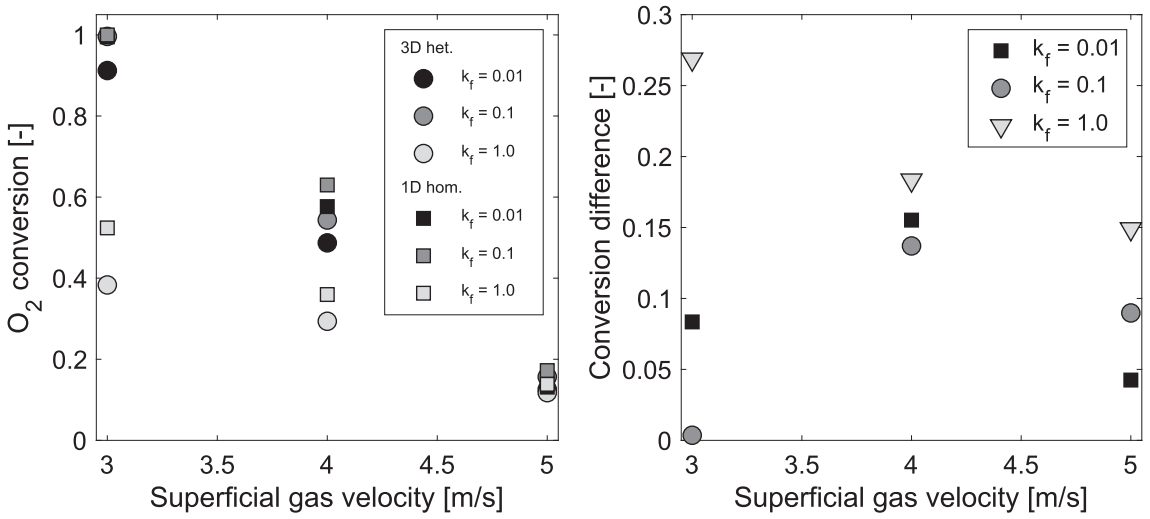

Fig. 14. Effects of fluidization velocity with different chemical reactivity values on the heterogeneous oxygen conversion and conversion difference between the assumptions.

fuel is elutriated out of the reactor even with the highest chemical reactivity values, which is indicative of limited time for mixing and reactions. The problem of low fluidization velocities is high accumulation of the fuel inventory, which in practice is not desired, for example due to increased pressure drop in the riser. The presented cases are not thus realistic, but rather aim to describe the phenomena involved. Obviously, the ratio of fuel to air should be controlled case dependently and dynamically to ensure stable reactor operations at acceptable pressure drop, temperature and conversion levels.

4. Conclusions and remarks

The studied small-scale calculation cases clearly indicate that the negligence of the heterogeneity leads to overestimation of local reaction rates up to 58% and overall conversion of the reactants up to 27%. The reactor average reaction rates are up to 31% higher with a 1D homogeneous model compared to heterogeneous results. Overestimation of reaction rates in the bottom region of the fluidized bed may lead to estimation of significantly higher bed temperatures and errors in other quantities affected by the reaction rates. As the reaction rates are heavily affected by, for example, the system geometry, fluidization regime, the properties of the fluid, bed material, and fuel, these results are case-specific but they illustrate the importance of acknowledging the heterogeneity that is inherent in gas–solid fluidized beds. As a result, the magnitude of differences affecting the process conditions and needed corrections should be investigated further as they are essential when developing and validating models that utilize approaches that contain significant simplifications. It is therefore important to acknowledge that there might be a large difference when modeling with reduced number of spatial dimensions or using large computational cells in three-dimensional modeling. These differences could be mitigated, for example, by applying correction functions.

Based on this study, the least affected by the heterogeneity are the cases with significant disproportioning between the reactants, i.e. lean fuel or oxygen cases. Moreover, in cases where the conversion is very low, negligence of heterogeneity does not produce significant differences in the results in the reactor-scale. In other cases, where the proportions of reactants are more comparable, the limitations of mixing are more apparent and their negligence leads to significantly higher differences between homogeneous and heterogeneous approaches.

The presented work contains several simplifications and assumptions. As the purpose of this research is to discuss the role of mixing, these simplifications were considered necessary to limit the complexity of the analysis and presentation. Future research could further study the role of the aspects neglected in this research, such as the effect of the local temperature levels on the local reaction rates. Additionally, future work could focus on providing generally applicable corrections to account for the heterogeneity in simplified models.

CRediT authorship contribution statement

Markku Nikku: Conceptualization, Investigation, Methodology, Software, Formal analysis, Writing - original draft. **Hadi Bordbar:** Methodology, Software. **Kari Myöhänen:** Methodology, Software.

Timo Hyppänen: Conceptualization, Supervision.

Declaration of Competing Interest

The authors declare that they have no known competing financial interests or personal relationships that could have appeared to influence the work reported in this paper.

Acknowledgements

This work was partly carried out within the Clustering Innovation Competence of Future Fuels in Power Production (CLIFF, 2014-2017) project as part of the activities of the Lappeenranta University of Technology, Finland. The authors would also like to acknowledge the financial support for this research from the Academy of Finland, Finland under Grant No. 278641.

Appendix 1: Models and parameters used in the kinetic theory for granular flow.

Model description	Reference
Gidaspow gas–solid momentum exchange $K_{sg} = \frac{3}{4} C_D \frac{\varepsilon_s \varepsilon_g \rho_g \mid \boldsymbol{v}_g - \boldsymbol{v}_s \mid}{d_s} \varepsilon_g^{-2.65} \quad \varepsilon_g > 0.8$	[45]
$C_D = \begin{cases} \frac{24}{Re_s}(1 + 0.15 Re_s^{0.687}) & Re_s \leqslant 1000 \\ 0.44 & Re_s > 1000 \end{cases}$	[45]
$K_{sg} = 150 \frac{\varepsilon_s (1-\varepsilon_g)\mu_g}{\varepsilon_g d_s^2} + 1.75 \frac{\rho_g \varepsilon_s \mid \boldsymbol{v}_g - \boldsymbol{v}_s \mid}{d_s} \quad \varepsilon_g \leqslant 0.8$	[45]
Symmetric Syamlal-ÓBrien solid–solid momentum exchange $K_{fb} = \frac{3(1+e_{ss})(\pi/2 + e_{fri}\pi^2/8)\varepsilon_b \varepsilon_f \rho_b \rho_f (d_b + d_f)^2 g_0 \mid \boldsymbol{v}_b - \boldsymbol{v}_f \mid}{2\pi(\rho_b d_b^3 + \rho_f d_f^3)}$	[46]
$g_0 = \left[1 - \left(\frac{\varepsilon_s}{\varepsilon_{s,max}}\right)^{1/3}\right]^{-1} + \frac{1}{2} d_i \sum_{l=1}^{N} \frac{\varepsilon_l}{d_l}$	[40]
Solid phase pressure $p_s = \varepsilon_s \rho_s \Theta_s [1 + 2(1 + e_{ss}) g_0 \varepsilon_s]$	[47]
Shear viscosity for solids phases: $\mu_s = \mu_{s,col} + \mu_{s,kin} + \mu_{s,fr}$	
$\mu_{s,col} = \frac{4}{5} \alpha_s \rho_s d_s g_{0,ss} (1 + e_{ss}) \sqrt{\frac{\Theta_s}{\pi}}$	[46]
$\mu_{s,kin} = \frac{\alpha_s \rho_s d_s \sqrt{\Theta_s \pi}}{6(3 - e_{ss})} \left[1 + \frac{2}{5}(1 + e_{ss})(3e_{ss} - 1)\alpha_s g_{0,ss}\right]$	[46]
$\mu_{s,fr} = \frac{p_{fr} \sin\phi}{2\sqrt{I_{2D}}}$	[48]
Bulk viscosity for solid phases $\lambda_s = \frac{4}{3} \varepsilon_s \rho_s d_s g_0 (1 + e) \sqrt{\frac{\theta_s}{\pi}}$	[47]
Conservation equation for the granular temperature $\frac{3}{2}\left[\frac{\partial}{\partial t}(\varepsilon_s \rho_s \theta_s) + \nabla \cdot (\varepsilon_s \rho_s \vec{v}_s \theta_s)\right] = (-\nabla p_s \bar{\bar{I}} + \bar{\bar{\tau}}_s) : \nabla \vec{v}_s + \nabla \cdot (\kappa_s \nabla \theta_s) - \gamma_s + \phi_{si}$	[47]
Collisional dissipation of energy $\gamma_{\Theta_s} = \frac{12(1 - e_{ss}^2) g_{0,ss}}{d_s \sqrt{\pi}} \alpha_s^2 \rho_s \Theta_s^{\frac{3}{2}}$	[47]
Exchange of kinetic energy between phases s and i : $\phi_{si} = -3 K_{si} \Theta_s$	[40]

References

[1] Scala F. Mass transfer around freely moving active particles in the dense phase of a gas fluidized bed of inert particles. Chem Eng Sci 2007;62:4159–76. https://doi.org/10.1016/J.CES.2007.04.040.

[2] Singh RI, Brink A, Hupa M. CFD modeling to study fluidized bed combustion and gasification. Appl Therm Eng 2013;52:585–614. https://doi.org/10.1016/j.applthermaleng.2012.12.017.

[3] Andrews LPN, Sundaresan S. Coarse-Grid Simulation of Gas-Particle Flows in Vertical Risers. Ind Eng Chem Res 2005;44:6022–37. https://doi.org/10.1021/ie0492193.

[4] Shah S, Myöhänen K, Kallio S, Ritvanen J, Hyppänen T. CFD modeling of gas–solids flow in a large scale circulating fluidized bed furnace. Powder Technol 2015;274:239–49. https://doi.org/10.1016/j.powtec.2015.01.019.

[5] Adamczyk WP, Myöhänen K, Hartge E-U, Ritvanen J, Klimanek A, Hyppänen T, et al. Generation of data sets for semi-empirical models of circulated fluidized bed boilers using hybrid Euler-Lagrange technique. Energy 2018;143:219–40. https://doi.org/10.1016/J.ENERGY.2017.10.029.

[6] Eri Q, Zhao X, Ranganathan P, Gu S. Numerical simulations on the effect of potassium on the biomass fast pyrolysis in fluidized bed reactor. Fuel 2017;197:290–7. https://doi.org/10.1016/J.FUEL.2017.01.109.

[7] Ghezelzhi MH, Wu H. Modelling of bio-oil steam gasification in a fluidized bed reactor. Fuel 2018;220:575–85. https://doi.org/10.1016/J.FUEL.2018.02.036.

[8] Chen Y, Grace JR, Zhao Y, Zhang J. Multi-fluid reactive modeling of sorption enhanced steam reforming of coke oven gas in fluidized bed. Fuel 2017;204:152–70. https://doi.org/10.1016/J.FUEL.2017.05.031.

[9] Taivassalo V, Peltola J, Kallio S. Time averaged CFD modelling of a circulating fluidized bed combustor. 21st Int. Conf. Fluid. Bed Combust. Proc. Vol. 2., 2012, p. 891.

[10] Nikku M, Myöhänen K, Ritvanen J, Hyppänen T, Lyytikäinen M. Three-dimensional modeling of biomass fuel flow in a circulating fluidized bed furnace with an experimentally derived momentum exchange model. Chem Eng Res Des 2016;115. https://doi.org/10.1016/j.cherd.2016.09.023.

[11] Shah S, Ritvanen J, Hyppänen T, Kallio S. Wall effects on space averaged two-fluid model equations for simulations of gas–solid flows in risers. Chem Eng Sci 2013;89:206–15. https://doi.org/10.1016/j.ces.2012.11.020.

[12] Peltola P, Ritvanen J, Tynjälä T, Hyppänen T. Fuel reactor modelling in chemical looping with oxygen uncoupling process. Fuel 2015;147:184–94. https://doi.org/10.1016/J.FUEL.2015.01.073.

[13] Lasheras A, Ströhle J, Galloy A, Epple B. Carbonate looping process simulation using a 1D fluidized bed model for the carbonator. Int J Greenh Gas Control 2011;5:686–93. https://doi.org/10.1016/J.IJGGC.2011.01.005.

[14] Seddighi S, Pallarès D, Johnsson F. One-dimensional modeling of oxy-fuel fluidized bed combustion for CO2 capture. 13th Int. Conf. Fluid., Gyeongju 2010.

[15] Seddighi S, Pallarès D, Normann F, Johnsson F. Carbon monoxide formation during oxy-fuel-fired fluidized-bed combustion. Energy Fuels 2013;27:2275–82.

[16] Sermyagina E, Saari J, Zakeri B, Kaikko J, Vakkilainen E. Effect of heat integration method and torrefaction temperature on the performance of an integrated CHP-torrefaction plant. Appl Energy 2015;149:24–34. https://doi.org/10.1016/J.APENERGY.2015.03.102.

[17] Shah S, Myöhänen K, Kallio S, Hyppänen T. CFD simulations of gas–solid flow in an industrial-scale circulating fluidized bed furnace using subgrid-scale drag models. Particuology 2015;18:66–75. https://doi.org/10.1016/j.partic.2014.05.008.

[18] Ates C, Selçuk N, Kulah G. Significance of particle concentration distribution on radiative heat transfer in circulating fluidized bed combustors. Int J Heat Mass Transf 2018;117:58–70. https://doi.org/10.1016/J.IJHEATMASSTRANSFER.2017.09.138.

[19] Frössling N. The evaporation of falling drops (in German). Gerlands Beiträge Zur Geophys 1938;52:170–216.

[20] Ranz WE, Marshall WR. Evaporation from drops: Part 1. Chem Eng Prog 1952;48:141–6.

[21] Ranz WE, Marshall WR. Evaporation from drops: Part 2. Chem Eng Prog 1952;48:173–80.

[22] Johnson CHJ. Heat transfer and mass transfer from the sphere at low reynolds numbers. Aust J Phys 1962;15:143–51.

[23] Rowe PN, Claxton KT, Lewis JB. Heat and mass transfer from a single sphere in an extensive flowing. Fluid 1965;43.

[24] Kunii D, Levenspiel O. Bubbling bed model for kinetic processes in fluidized beds. Gas-solid mass and heat transfer and catalytic reactions. Ind Eng Chem Process Des Dev 1968;7:481–92. https://doi.org/10.1021/i260028a001.

[25] Gunn DJ. Transfer of heat or mass to particles in fixed and fluidised beds. Int J Heat

Mass Transf 1978;21:467–76. https://doi.org/10.1016/0017-9310(78)90080-7.
[26] La Nauze RD, Jung K. The kinetics of combustion of petroleum coke particles in a fluidized-bed combustor. Symp Combust 1982;19:1087–92. https://doi.org/10.1016/S0082-0784(82)80284-1.
[27] Breault RW. A review of gas–solid dispersion and mass transfer coefficient correlations in circulating fluidized beds. Powder Technol 2006;163:9–17. https://doi.org/10.1016/J.POWTEC.2006.01.009.
[28] Breault RW, Guenther CP. Mass transfer in the core-annular and fast fluidization flow regimes of a CFB. Powder Technol 2009;190:385–9. https://doi.org/10.1016/J.POWTEC.2008.08.021.
[29] Breault RW, Guenther C. Mass transfer coefficient prediction method for CFD modeling of riser reactors. Powder Technol 2010;203:33–9. https://doi.org/10.1016/J.POWTEC.2010.03.024.
[30] Zevenhoven R, Järvinen M. Particle/turbulence interactions, mass transfer and gas/solid chemistry in a CFBC riser. Flow Turbul Combust 2001;67:107–24. https://doi.org/10.1023/A:1014023320280.
[31] Vollert J, Werther J. Mass transfer and reaction behaviour of a circulating fluidized bed reactor. Chem Eng Technol 2018;17:201–9. https://doi.org/10.1002/ceat.270170309.
[32] Cloete S, Johansen ST, Amini S. An assessment of the ability of computational fluid dynamic models to predict reactive gas-solid flows in a fluidized bed. Powder Technol 2012;215–216:15–25. https://doi.org/10.1016/j.powtec.2011.08.033.
[33] Shuyan W, Lijie Y, Huilin L, Long Y, Bouillard J, Zhenhua H. Numerical analysis of interphase heat and mass transfer of cluster in a circulating fluidized bed. Powder Technol 2009;189:87–96. https://doi.org/10.1016/J.POWTEC.2008.06.011.
[34] Kashyap M, Gidaspow D. Computation and measurements of mass transfer and dispersion coefficients in fluidized beds. Powder Technol 2010;203:40–56. https://doi.org/10.1016/J.POWTEC.2010.03.025.
[35] Carlos Varas ÁE, Peters EAJF, Kuipers JAM. Computational fluid dynamics-discrete element method (CFD-DEM) study of mass-transfer mechanisms in riser flow. Ind Eng Chem Res 2017;56:5558–72. https://doi.org/10.1021/acs.iecr.7b00366.
[36] Lu J, Das S, Peters EAJF, Kuipers JAM. Direct numerical simulation of fluid flow and mass transfer in dense fluid-particle systems with surface reactions. Chem Eng Sci 2018;176:1–18. https://doi.org/10.1016/J.CES.2017.10.018.
[37] Rodrigues SS, Forret A, Montjovet F, Lance M, Gauthier T. Riser hydrodynamic study with different Group B powders. Powder Technol 2015;272:300–8. https://doi.org/10.1016/j.powtec.2014.12.014.
[38] Khorshidi J, Zarei T, Davari H. A detailed model for combustion characteristics of petroleum residue and heat transfer coefficients in a CFB combustor. Pet Sci Technol 2016;34:1340–4. https://doi.org/10.1080/10916466.2016.1202974.
[39] Dell Orco S, Rizzo AM, Buffi M, Chiaramonti D. Design of a Circulating Fluidized Bed Combustor for Lignin- Rich Residue Derived From Second-Generation Bioethanol Production Plant. Chem Eng Trans 2018;65:277-282 SE-Research Articles. doi:10.3303/CET1865047.
[40] Ansys Inc. Ansys Fluent Theory Guide. 2018.
[41] Vepsäläinen A, Shah S, Ritvanen J, Hyppänen T. Bed Sherwood number in fluidised bed combustion by Eulerian CFD modelling. Chem Eng Sci 2013;93:206–13. https://doi.org/10.1016/J.CES.2013.01.065.
[42] Shah S, Ritvanen J, Hyppänen T, Kallio S. Space averaging on a gas–solid drag model for numerical simulations of a CFB riser. Powder Technol 2012;218:131–9. https://doi.org/10.1016/j.powtec.2011.11.053.
[43] Nikku M, Jalali P, Hyppänen T. Comparison of Ansys Fluent and OpenFOAM is simulation of circulating fluidized bed riser. In: Nowak W, Marek S, Pawel M, editors. Proc. 12th Int. Conf. Fluid. Bed Technol., Krakow: 2017, p. 349–56.
[44] Nikku M, Daikeler A, Stroh A, Myöhänen K. Comparison of solid phase closure models in Eulerian-Eulerian simulations of a circulating fluidized bed riser. Chem Eng Sci 2019;195:39–50. https://doi.org/10.1016/J.CES.2018.11.031.
[45] Gidaspow D, Bezburuah R, Ding J. Hydrodynamics of circulating fluidized beds: Kinetic theory approach. 7th Int. Conf. Fluid. Gold Coast 1991.
[46] Syamlal M, Rogers W, O'Brien TJ. MFIX documentation theory guide 1993;1004. doi:10.2172/10145548.
[47] Lun CKK, Savage SB, Jeffrey DJ, Chepurniy N. Kinetic theories for granular flow: inelastic particles in couette flow and slightly inelastic particles in a general flow field. J Fluid Mech 1984;140:223–56.
[48] Schaeffer DG. Instability in the evolution equations describing incompressible granular flow. J Differ Equ 1987;66:19–50.